

# Gaussian Process-Based Extended Object Estimation for 6G ISAC at Millimeter-Wave Frequencies

M. Ertug Pihtili<sup>†</sup>, Ossi Kaltiokallio<sup>†</sup>, Julia Equi<sup>‡</sup>, Jukka Talvitie<sup>†</sup>, Elena Simona Lohan<sup>†</sup>, Ertugrul Basar<sup>†</sup>, and Mikko Valkama<sup>†</sup>

<sup>†</sup>Tampere Wireless Research Center, Electrical Engineering Unit, Tampere University, Tampere, Finland

<sup>‡</sup>Ericsson Research, Jorvas, Finland

**Abstract**—This paper introduces a Gaussian process (GP)-based method for extended object estimation (EOE) in integrated sensing and communication (ISAC) scenarios, representing a promising approach to enhance environmental awareness beyond the conventional point-scatterer assumption. The suitability of the proposed GP-based method for EOE is investigated through a practical measurement setup compliant with the fifth-generation (5G) New Radio (NR) standard and employing bistatic sensing, with results evaluated for both mapping and simultaneous localization and mapping (SLAM) cases at millimeter-wave (mmWave) frequencies. The findings reveal that the enhanced capabilities of communication networks, when combined with bistatic sensing and GP-based EOE, enable improved environmental awareness in future wireless systems. Importantly, the results demonstrate that, under practical conditions, GP effectively performs EOE in both mmWave mapping and SLAM scenarios.

**Index Terms**—Bistatic Sensing, Experimental Data, Extended Object, Gaussian Processes, ISAC, mmWave, Shape Estimation.

## I. INTRODUCTION

The sixth-generation (6G) wireless systems will be capable of perceiving the environment by incorporating sensing into the network, in addition to providing enhanced communication functionalities [1]. In this context, orthogonal frequency-division multiplexing (OFDM) is a promising waveform, as it can serve both sensing and communication purposes. Notably, OFDM combined with multiple-input multiple-output (MIMO) at millimeter-wave (mmWave) frequencies enables advanced sensing capabilities due to the increased bandwidth and larger array apertures, providing high resolution in both the delay and angular domains and allowing for resolvable multipath components. Consequently, the integrated sensing and communication (ISAC) paradigm will be a key enabler of functionalities such as localization, mapping, and simultaneous localization and mapping (SLAM), thereby bringing enhanced environmental awareness to future wireless networks [1].

In this context, conventional point-scatterer environmental object (or target) models assume that each multipath component originates from a single point object, referred to as a landmark in the environment. However, the high-resolution sensing capabilities of ISAC systems make it possible to move beyond this assumption by resolving multiple incidence points (IPs) originating from the same object, known as an extended object [2]. Consequently, non-line-of-sight (NLoS) paths can

be exploited to enhance environmental awareness by sensing both active and passive objects, along with their physical characteristics such as shape, size, and material type [3].

An extended object refers to an object that generates multiple resolvable multipath rays when illuminated by a radio frequency (RF) signal, thereby enabling the estimation of its spatial extent. In [4], extended object estimation (EOE) was performed by extracting the convex hull through a proposed post-processing scheme, which enhances landmark reconstruction and enables outlier removal for radio mapping, along with user equipment (UE) localization, within a bistatic sensing system framework. In [2], a novel multipath-based SLAM algorithm was proposed, incorporating the shape estimation of various object types through a constructed measurement model. Furthermore, [5] introduced a multiple-model probability hypothesis density (PHD)-based SLAM algorithm, which exploits both the measurements and the labels of the PHD filter for offline estimation of extended objects, such as reflecting surfaces and scattering objects, with results validated using practical measurements. Apart from environmental mapping and SLAM, [6] proposed a target tracking algorithm based on a random hypersurface model (RHM) for estimating star-convex shapes of extended objects, in addition to the commonly used ellipse assumptions. Additionally, [7] introduced an extended target tracking scheme in which the shape of the extended target is estimated using Gaussian process (GP). Herein, GP is a non-parametric Bayesian extension of linear regression, characterized by an infinitely long mean vector and an infinite-by-infinite covariance matrix, where any finite subset follows a joint Gaussian distribution [8]. While prior works have addressed EOE in the ISAC literature, the experimental validation of GP-based EOE in practical ISAC scenarios remains unexplored, which motivates this work.

In this work, the suitability of GP in ISAC systems for EOE using mmWave experimental data is investigated. The experiments are conducted using a fifth-generation (5G) new radio (NR) setup, where the transmitter (Tx) employs an OFDM waveform and transmits 5G NR standard-compliant beam-based positioning reference signals (PRSs) at 60 GHz. The experimental data are utilized for both mmWave mapping and SLAM scenarios, in which the estimated IPs of single-bounce non-line-of-sight (NLoS) paths are subsequently used

to approximate the contour of objects in the measurement environment by leveraging GPs, following the proposed method. Unlike the opportunistic case, where measurement points are assumed to originate from the entire contour of the object, the practical data capture only a portion of each object with a limited number of measurements. The findings indicate that, when combined with ISAC systems, GPs enable reliable estimation of object shapes even under limited measurement conditions, thereby enhancing environmental awareness.

*Notation:* Italic lowercase letters  $x$  denote scalars, bold lowercase letters  $\mathbf{x}$  denote vectors, and bold uppercase letters  $\mathbf{X}$  denote matrices. Complex- and real-valued vectors or matrices of size  $a \times b$  are denoted by  $\mathbb{C}^{a \times b}$  and  $\mathbb{R}^{a \times b}$ , respectively. The operator  $(\cdot)^T$  represents transpose, and  $\exp(x)$  is the exponential function. A real Gaussian distribution with zero mean and variance  $\sigma^2$  is written as  $\mathcal{N}(0, \sigma^2)$ . The  $N \times N$  identity matrix is denoted by  $\mathbf{I}_N$ , the norm by  $\|\cdot\|$ , and expectation by  $\mathbb{E}[\cdot]$ . Finally,  $\mathbf{1}_N$  denotes an all-ones vector of size  $N \times 1$ .

## II. ENVIRONMENTAL SENSING

We consider a bistatic sensing scenario in which the Tx location  $\mathbf{p}_{\text{TX}} \in \mathbb{R}^2$  and orientation  $\alpha_{\text{TX}}$  are known, the IP of the  $i$ th propagation path is unknown  $\mathbf{p}_i \in \mathbb{R}^2$ , and the receiver (Rx) state is represented by  $\mathbf{s}_{\text{RX}} = [\mathbf{p}_{\text{RX}}, \alpha_{\text{RX}}, b_{\text{RX}}]^T \in \mathbb{R}^4$  which consists of the position, heading, and clock bias between the unsynchronized Tx and Rx clocks. In the following, we summarize two methods for estimating  $\mathbf{p}_i$ 's using the channel parameter estimates  $\mathbf{z}_i$ 's and the (un)known Rx state. The estimated IPs are then used by the GP-based EOE method described in Section III-B.

### A. System Model

We consider beam-based OFDM transmission where beam sweeping is utilized at both Tx and Rx, equipped with antenna arrays. Assuming a time-invariant channel response over one OFDM symbol, and sampling timing accuracy within the period of a cyclic prefix, the received sample of the  $l$ th OFDM-symbol and  $k$ th subcarrier for the  $m$ th Tx beam and  $n$ th Rx beam can be written as [9]

$$y_{k,l}^{m,n} = \sum_{i=0}^N \xi_i G_{\text{TX}}^m(\phi_i) G_{\text{RX}}^n(\theta_i) e^{-j2\pi k \Delta f \tau_i} x_{k,l}^{m,n} + w_{k,l}^{m,n}, \quad (1)$$

where  $\xi_i$ ,  $\tau_i$ ,  $\phi_i$ ,  $\theta_i$  are the complex path coefficient, time-of-arrival (ToA), angle-of-departure (AoD), and angle-of-arrival (AoA) for the  $i$ th propagation path, respectively. Furthermore,  $\Delta f$  denotes the subcarrier spacing,  $x_{k,m} \in \mathbb{C}$  with  $|x_{k,m}| = 1 \forall k, m$  is the transmitted PRS sample, and  $w_{k,l}^{m,n}$  represents noise affected by the Rx beam. The total number of paths is  $N + 1$ , where  $N$  is the number of NLoS propagation paths, and the path index  $i = 0$  is reserved for the line-of-sight (LoS) path, if present and detected. The effects of steering vectors and beamformers are captured by  $G_{\text{TX}}^m(\phi_i) \in \mathbb{C}$  and  $G_{\text{RX}}^n(\theta_i) \in \mathbb{C}$ , which describe angular responses of the  $m$ th Tx beam and  $n$ th Rx beam, respectively. Depending on the

knowledge of  $G_{\text{TX}}^m(\phi_i)$  and  $G_{\text{RX}}^n(\theta_i)$ , channel estimation can be implemented in multiple ways [9], [10].

### B. mmWave Mapping

Let  $\mathbf{z}_i = [\tau_i, \phi_i, \theta_i]^T$  denote the channel parameter estimate of the  $i$ th propagation path. Assuming  $\mathbf{z}_i$  are unbiased and Gaussian, the likelihood function of the single-bounce propagation paths is [11]:

$$p(\mathbf{z}_i | \mathbf{s}_{\text{RX}}, \mathbf{p}_i) = \mathcal{N}(\mathbf{z}_i | \mathbf{g}(\mathbf{s}_{\text{RX}}, \mathbf{p}_i), \mathbf{R}_i), \quad (2)$$

where  $\mathbf{R}_i = \text{diag}([1 \text{ ns}, 1 \text{ deg}, 1 \text{ deg}]) \forall i$  is the covariance matrix and the mean is given by

$$\mathbf{g}(\mathbf{s}_{\text{RX}}, \mathbf{p}_i) = \begin{bmatrix} \|\mathbf{p}_{\text{TX}} - \mathbf{p}_i\|/c + \|\mathbf{p}_i - \mathbf{p}_{\text{RX}}\|/c + b_{\text{RX}} \\ \text{atan2}(y_i - y_{\text{TX}}, x_i - x_{\text{TX}}) - \alpha_{\text{TX}} \\ \text{atan2}(y_i - y_{\text{RX}}, x_i - x_{\text{RX}}) - \alpha_{\text{RX}} \end{bmatrix}, \quad (3)$$

which describes the geometric relationship between the Tx, Rx and IP. In the above,  $c$  denotes the speed of light, and  $\text{atan2}(\cdot, \cdot)$  is the two-argument arctangent. Now, the IPs can be estimated independently for every propagation path, by solving the following nonlinear optimization problem

$$\hat{\mathbf{p}}_i = \arg \min_{\mathbf{p}_i} J(\mathbf{s}_{\text{RX}}, \mathbf{p}_i), \quad i = 1, \dots, N, \quad (4)$$

where  $J(\mathbf{s}_{\text{RX}}, \mathbf{p}_i) = (\mathbf{z}_i - \mathbf{g}(\mathbf{s}_{\text{RX}}, \mathbf{p}_i))^T \mathbf{R}_i^{-1} (\mathbf{z}_i - \mathbf{g}(\mathbf{s}_{\text{RX}}, \mathbf{p}_i))$  is a quadratic cost function. It is to be noted that the described mapping method assumes  $\mathbf{s}_{\text{RX}}$  is known.

### C. mmWave Simultaneous Localization and Mapping

SLAM aims to solve the unknown Rx state and IP locations using a set of channel parameter estimates,  $\mathcal{Z} = \{\mathbf{z}_0, \mathbf{z}_1, \dots, \mathbf{z}_N\}$ . The unknown parameters can be estimated if a sufficient number of single-bounce NLoS paths exist since each provides three additional known parameters (i.e.,  $\mathbf{z}_i$ ), while being parameterized by two unknowns (i.e.,  $\mathbf{p}_i$ ). To solve the SLAM problem, we resort to a robust snapshot SLAM algorithm described in [11]. The algorithm employs a random sample consensus (RANSAC)-inspired least squares (LS) approach, in which the method first utilizes a minimal subset of  $\mathcal{Z}$  to compute an initial solution  $\tilde{\mathbf{s}}_{\text{RX}}$ . Then, based on  $\tilde{\mathbf{s}}_{\text{RX}}$  and an error metric,  $\mathcal{Z}$  is partitioned into a set of inliers (i.e., LoS and single-bounce NLoS) and outliers (i.e., multi-bounce NLoS and clutter). Thereafter, the problem is resolved using the inlier set and the final Rx estimate  $\hat{\mathbf{s}}_{\text{RX}}$  is the one that minimizes the LS cost. Lastly,  $\hat{\mathbf{p}}_i$ 's are computed independently for every inlier using (4) and  $\hat{\mathbf{s}}_{\text{RX}}$ . For further details, see [11].

## III. GP-BASED EXTENDED OBJECT ESTIMATION

### A. Creating Training Dataset for GP-based EOE

In order to perform GP-based EOE, the estimated IPs are first clustered by utilizing the density-based spatial clustering of applications with noise (DBSCAN) algorithm [12]. Let  $\hat{\mathbf{p}}_i^c = [x_i^c, y_i^c]^T$ ,  $i \in \mathcal{I}_c$  denote the cluster IPs which ideally capture the contour of the extended object and let  $\mathcal{I}_c$  denote the set of indices of cluster  $c$  computed using DBSCAN. Since

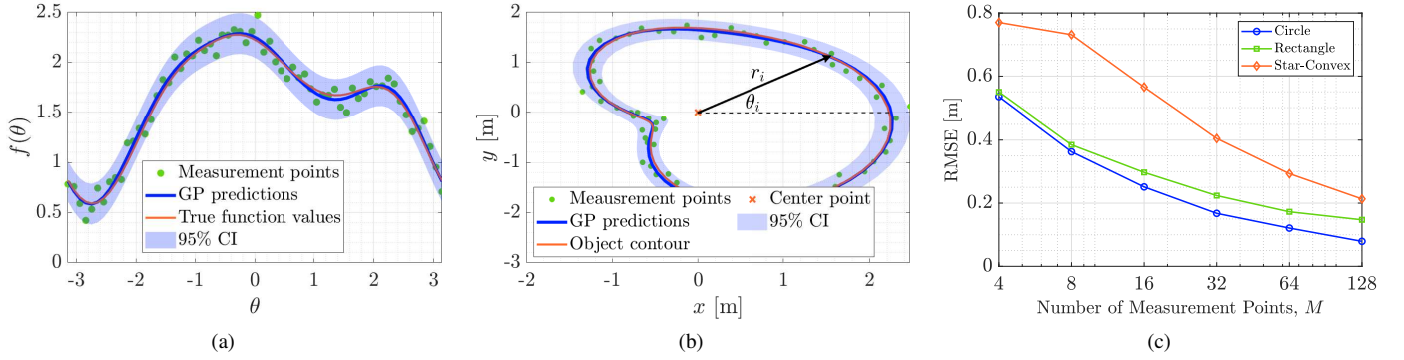


Fig. 1. Star-convex EOE using GP with  $M = 64$  noisy contour measurements. The ground-truth parameters are  $\beta = [4.0, 4.0, 1.0, 0.01]$ , while the estimated optimal values  $\hat{\beta} = [0.9038, 0.3622, 1.6198, 0.0091]$  which are obtained by maximizing (13). (a) Predicted function values with measurement points and the 95% confidence interval (CI). (b) Reconstructed star-convex object showing both ground-truth and predicted contours. (c) RMSE performance for different extended objects versus the number of measurement points  $M$ .

the GP-based method describes the extended objects as star-convex shapes using a radial function [7],  $\hat{\mathbf{p}}_i^c$  are converted from the Euclidean coordinate system to the polar coordinate system as

$$\begin{bmatrix} \theta_i^c \\ r_i^c \end{bmatrix} = \begin{bmatrix} \text{atan2}(y_i^c - \bar{y}^c, x_i^c - \bar{x}^c) \\ \sqrt{(x_i^c - \bar{x}^c)^2 + (y_i^c - \bar{y}^c)^2} \end{bmatrix}, \quad (5)$$

where  $\bar{x}^c = \frac{1}{M_c} \sum_{i \in \mathcal{I}_c} x_i^c$  and  $\bar{y}^c = \frac{1}{M_c} \sum_{i \in \mathcal{I}_c} y_i^c$  denote the cluster centers, and  $M_c = |\mathcal{I}_c|$  cardinality of the set. In the next section, angles  $\theta_i^c \in [-\pi, \pi]$  are used as training inputs (regressors) and radial distances  $r_i^c$  are used as outputs (observations) of the GP regression model. Thus, collecting all regressors and observations in the cluster yields the training dataset used in GP-based EOE, mathematically given by

$$\mathcal{D}_c = \left\{ [\theta_i^c, r_i^c]^\top \in \mathbb{R}^2 \mid i \in \mathcal{I}_c \right\}. \quad (6)$$

### B. Extended Object Estimation Using Gaussian Processes

In the following, GP-based EOE is performed independently for every cluster  $\mathcal{D}_c$  and dependence of cluster  $c$  is excluded from the notation for brevity. Now considering dataset  $\mathcal{D}$  which represents the contour of an extended object, the noisy radial observations can be defined as [7]

$$r_i = f(\theta_i) + n_i, \quad (7)$$

where  $f(\theta_i)$  is the radial function which we seek to estimate using GP regression, and  $n_i \sim \mathcal{N}(0, \sigma_n^2)$  denotes zero-mean independent and identically distributed (i.i.d.) observation noise. Hence, the input–output mapping through the radial function  $f(\theta_i)$  is modeled as a GP that maps polar angles to radial distances for two-dimensional (2D) object shape estimation, expressed as

$$f(\theta_i) \sim \mathcal{GP}(m(\theta_i), k(\theta_i, \theta_{i'})), \quad (8)$$

where the mean function  $m(\theta_i)$  represents the average radius of the target contour and  $k(\theta_i, \theta_{i'})$  is the covariance function which captures similarity between different function values. The GP is fully characterized by its mean,  $\mathbb{E}[f(\theta_i)] = m(\theta_i)$ , and its covariance function,  $\mathbb{E}[(f(\theta_i) - m(\theta_i))(f(\theta_{i'}) - m(\theta_{i'}))] = k(\theta_i, \theta_{i'})$ , where a periodic squared exponential

covariance function with periodicity  $2\pi$  is employed to capture the star-convex shape of the object, given by [7]

$$k(\theta_i, \theta_{i'}) = \sigma_f^2 \exp\left(-\frac{2 \sin^2\left(\frac{\|\theta_i - \theta_{i'}\|}{2}\right)}{\ell^2}\right). \quad (9)$$

Therein, the covariance function quantifies the correlation among input points, and tuning its hyperparameters is essential for accurately modeling the input–output mapping. The hyperparameters in (9) are as follows:  $\sigma_f$  is the magnitude scale, which controls the amplitude of the function; and  $\ell$  is the characteristic length scale, which determines the rate of variation of the function.

GP regression learns the values of  $f(\theta_i)$  from the training inputs and predicts values for new test inputs  $\theta_*$  by defining a distribution over functions. In principle, one could generate functions from the prior distribution  $f(\theta_*) \sim \mathcal{N}(m(\theta_*), k(\theta_*, \theta_*))$  and discard those inconsistent with the data. However, this is not computationally feasible since there may be infinitely many such functions. Instead, the posterior distribution is obtained by combining the prior with the data, yielding [8]

$$p(f(\theta_*) \mid \theta_*, \mathcal{D}) = \mathcal{N}(f(\theta_*) \mid \mathbb{E}[f(\theta_*)], \mathbb{V}[f(\theta_*)]). \quad (10)$$

As a result, the posterior leads to the key predictive equations of the GP, namely the predictive mean and predictive variance, which are given respectively as [8]

$$\mathbb{E}[f(\theta_*)] = \mu_* + \mathbf{k}_*^\top (\mathbf{K} + \sigma_n^2 \mathbf{I}_M)^{-1} (\mathbf{r} - \boldsymbol{\mu}), \quad (11)$$

$$\mathbb{V}[f(\theta_*)] = k(\theta_*, \theta_*) - \mathbf{k}_*^\top (\mathbf{K} + \sigma_n^2 \mathbf{I}_M)^{-1} \mathbf{k}_*. \quad (12)$$

In the above,  $M = |\mathcal{D}|$  is the number of training points in the cluster,  $\mathbf{r} = [r_1, r_2, \dots, r_M]^\top$ ,  $[\mathbf{K}]_{ij} = k(\theta_i, \theta_j)$  and  $\mathbf{k}_*$  is an  $M$ -dimensional vector with the  $i$ th element being  $[\mathbf{k}_*]_i = k(\theta_*, \theta_i)$ . The mean of the radial function  $\mu$  is learned from data such that  $\mu_* = \mu$  and  $\boldsymbol{\mu} = \mathbf{1}_M \mu$ .

In practice, to obtain an accurate estimate for  $f(\theta_*)$ , the model parameters (mean  $\mu$  and hyperparameters  $\beta = [\sigma_f^2, \ell^2, \sigma_n^2]^\top$ ) should also be learned from data which can be achieved by maximizing the log marginal likelihood. The log marginal likelihood is given by

$$p(\mathbf{r} \mid \mu, \beta) = -\frac{1}{2} \boldsymbol{\eta}^\top \mathbf{K}_y^{-1} \boldsymbol{\eta} - \frac{1}{2} \log |\mathbf{K}_y| - \frac{M}{2} \log 2\pi, \quad (13)$$

where  $\boldsymbol{\eta} = \mathbf{r} - \boldsymbol{\mu}$  and  $\mathbf{K}_y = \mathbf{K} + \sigma_n^2 \mathbf{I}_M$ . The partial derivatives of the log marginal likelihood are:

$$\frac{\partial \log p(\mathbf{r} | \boldsymbol{\mu}, \boldsymbol{\beta})}{\partial \boldsymbol{\mu}} = \mathbf{1}_M^\top \mathbf{K}_y^{-1} \boldsymbol{\eta}, \quad (14)$$

$$\frac{\partial \log p(\mathbf{r} | \boldsymbol{\mu}, \boldsymbol{\beta})}{\partial \beta_j} = \frac{1}{2} \text{tr} \left[ (\boldsymbol{\alpha} \boldsymbol{\alpha}^\top - \mathbf{K}_y^{-1}) \frac{\partial \mathbf{K}_y}{\partial \beta_j} \right], \quad (15)$$

where  $\boldsymbol{\alpha} = \mathbf{K}_y^{-1} \boldsymbol{\eta}$ . Given the log marginal likelihood and its derivatives, the model parameters can now be trained, for example, using a gradient-based optimizer.

### C. GP-based EOE Example Using Synthetic Data

Figs. 1(a) and 1(b) illustrate GP-based EOE of a 2D star-convex shape based on  $M = 64$  noisy radial observations which are generated synthetically. The GP model parameters are trained by maximizing (13) and the predictive mean and variance are computed using (11) and (12), respectively. The estimated radial function and the 95% confidence interval (CI), corresponding to the pointwise mean  $\pm 2$  standard deviations, are shown in Fig. 1(a). Since the measurements cover the full object contour, the complete star-convex shape is predicted accurately as illustrated in Fig. 1(b).

To demonstrate the effectiveness of GP-based EOE, Fig. 1(c) shows the root mean square error (RMSE) between the true and predicted radial function values (in meters) for three basic extended objects under varying numbers of measurement points  $M$ , where the measurements are synthetically generated along the object contours. The RMSE is defined as  $\text{RMSE} = \sqrt{\frac{1}{M} \sum_{i=1}^M (f(\theta_i) - \mathbb{E}[f(\theta_i)])^2}$ , and the results are averaged over  $10^3$  Monte Carlo iterations. As observed, increasing the number of measurement points improves estimation performance in all cases, since more points provide more comprehensive information about the underlying input–output mapping. The results further demonstrate the robustness of GP-based extended object estimation, as reliable approximations of the object contours are obtained even when the number of measurement points  $M$  is small.

## IV. GP-BASED EOE USING MMWAVE MEASUREMENTS

In this section, the 2D EOE using GPs with empirical mmWave measurements is presented for both the mapping and SLAM scenarios. The measurements were conducted at the Hervanta Campus of Tampere University, Finland, inside the Campus Arena building, which features a large, partially open space with various environmental objects, including pillars and walls. The indoor mmWave measurements were obtained from 5G NR standard-compliant beam-based PRS transmissions with a bandwidth of 400 MHz [13], where the Tx transmits an OFDM waveform at 60 GHz, and the Rx follows a trajectory while collecting beamformed PRS signals for environmental sensing. Both the Tx and Rx are equipped with 4  $\times$  16 uniform planar arrays (UPAs). More details on the measurement campaign and setup can be found in [9].

Upon estimating the IPs either using mapping or SLAM, the IPs are first clustered using the DBSCAN algorithm as described in Section III-A, resulting in seven clusters, each representing a

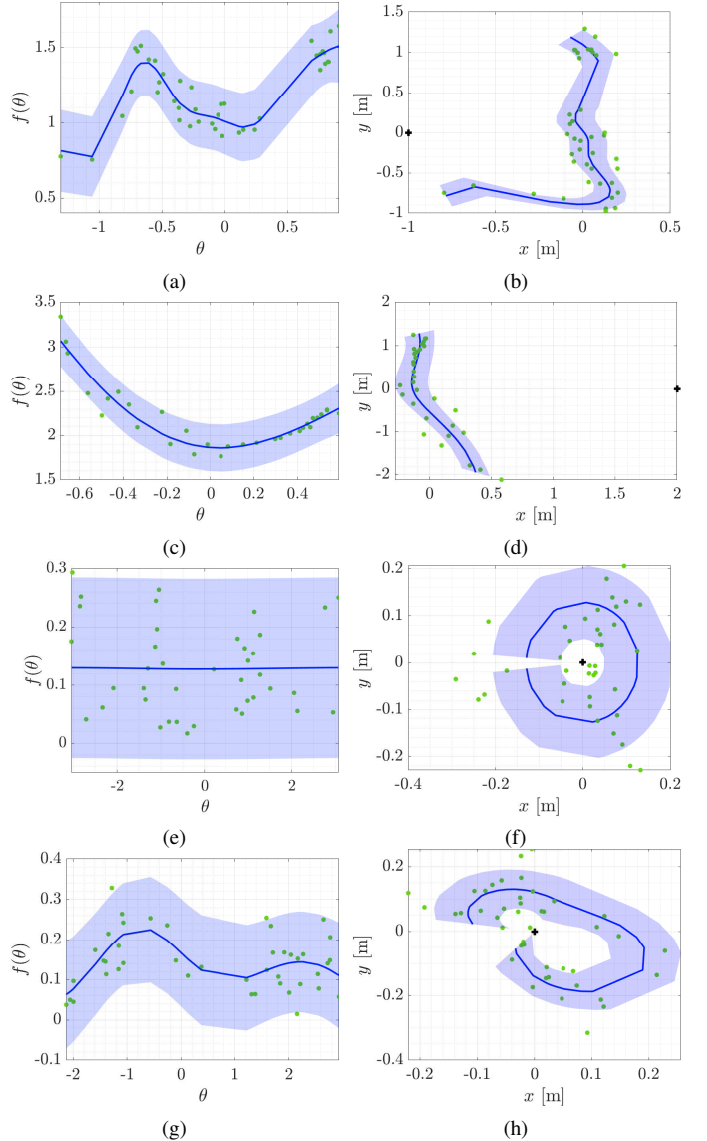


Fig. 2. (a), (c), (e), and (g) show the predictive mean functions in the radial domain, while (b), (d), (f), and (h) present the estimated object shapes in the Cartesian coordinate system for clusters 1, 2, 3, and 4, respectively. The legend indicates: — GP Predictions, + Object Center, • Measurement Points, ■ %95 Confidence Interval.

set of measurement points corresponding to an object contour. Specifically, clusters 1, 2, 5, and 8 correspond to walls, while clusters 3, 4, and 6 correspond to pillars, as shown in Fig. 3(a). Subsequently, the created training datasets  $\mathcal{D}_c$  are used for GP-based EOE as presented in Section III-B. For each cluster, the best inputs are selected as  $\hat{\lambda}_i = \lambda_i$ , and the hyperparameters are initialized as  $\hat{\sigma} = 2$ ,  $\hat{\sigma}_f = 2$ ,  $\hat{\sigma}_n = 2$ , and  $\hat{\tau} = \mathbb{E}[r]$  which denotes the mean radial distance of each cluster. The hyperparameters are then optimized by maximizing (13) to obtain the radial function  $f(\cdot)$  that best explains the input–output mapping. Furthermore, to better represent the wall geometries, biases are applied to the centroids of clusters 1, 2, and 7, defined as  $[\Gamma_1; 0]$ ,  $[\hat{a}; 0]$ , and  $[\Gamma_0; 2; \Gamma_1]$ , respectively.

Fig. 2 presents the GP-based EOE results along with the

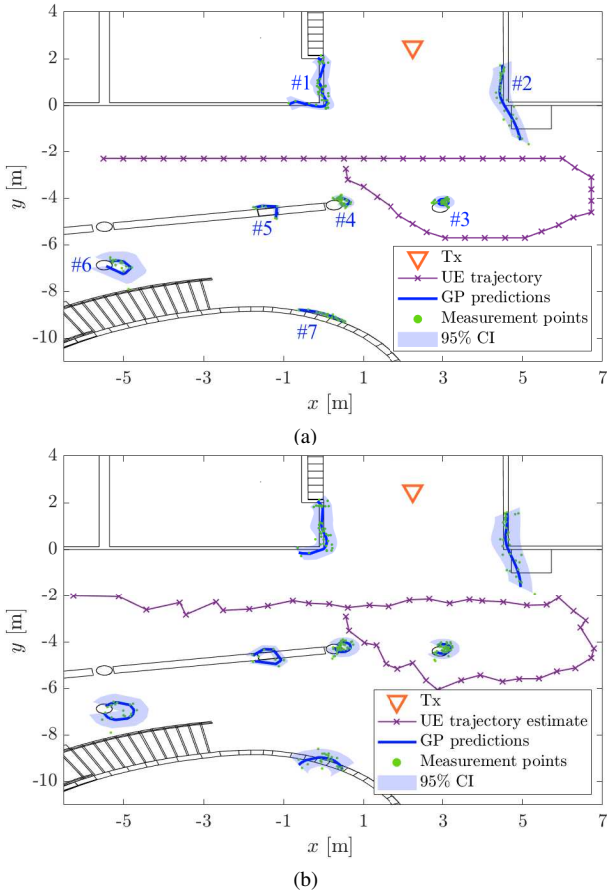


Fig. 3. (a) EOE using GP for mmWave mapping scenario. (b) EOE using GP for mmWave SLAM scenario.

predicted mean functions in (11) for the mapping dataset, shown for clusters 1, 2, 3, and 4, respectively. In this context,  $f(\theta)$  is a smooth function and ideally constant for circular shapes, meaning that test inputs enable the estimation of objects with smooth radial functions, such as clusters 3 and 4, even when only partial contour information is available. In contrast, objects with more complex geometries, such as walls, may exhibit rapidly varying radial functions  $f(\theta)$ , making estimation more challenging under limited data, as observed for clusters 1 and 2. For instance, the optimized characteristic length-scale values of cluster 1 (a wall) and cluster 3 (a pillar) are  $\ell_1 = 0.2343$  and  $\ell_3 = 1.3129$  for the mapping dataset. A smaller  $\ell$  indicates faster variations in  $f(\theta)$ , as  $\ell$  determines the distance over which the function changes significantly.

Ultimately, Fig. 3 illustrates the GP prediction results for the empirical mmWave measurements, together with the map of the sensing environment. Comparing Figs. 3(a) and 3(b), in the mapping scenario, the Rx position and ground-truth trajectory are known, whereas in the SLAM scenario, the Rx location is unknown and its trajectory is estimated. Although the IP estimates in the SLAM scenario are less accurate than those in the mapping case, the overall performance of both scenarios remains comparable, indicating that the GP-based EOE performs well in both settings. It is important to emphasize that the predictive capability of GP is inherently

constrained by both the number of measurement points and the angular coverage of the sampled object contours, since in both scenarios, the measurement points do not cover the entire object contour. Consequently, the training inputs, i.e., the polar angles  $\theta_i$ , represent only the portions of the objects that were sampled, which reflects a practical scenario as capturing the full contour with a single Tx–Rx pair is often infeasible. Even with partial information, the shapes of the pillars (clusters 3, 4, and 6), which correspond to circles in 2D, can still be accurately predicted. The GP model provides only coarse estimates of the wall extents based on the available measurement points, indicating that clusters 1 and 2 require additional measurements spanning a wider angular range of the object contour for improved EOE performance, a limitation that can be mitigated by employing multiple Tx–Rx pairs to capture the full object contours.

## V. CONCLUSION

This paper has presented a GP-based EOE approach using practical mmWave data, where the measurement setup follows 5G NR standards. The results demonstrate that object shapes in the environment can be either finely or coarsely estimated depending on the object geometry and the availability of measurement data along the object contour. When combined with the environmental sensing capabilities of ISAC systems, GP provides valuable information about the surrounding environment, and the estimated extended objects can be further leveraged for ISAC applications by offering more concrete structural insights compared to conventional methods that rely on point scatterer assumptions. This information can be used for environmental mapping and for identifying static objects along with their shapes, which can subsequently enhance clutter cancellation algorithms in ISAC systems, leading to more accurate sensing performance than approaches based on point-scatterer models.

## ACKNOWLEDGEMENT

This work was funded by the EU Horizon Europe MSCA (MiFuture, Grant No. 101119643) on ultra-massive MIMO for future cell-free heterogeneous networks.

## REFERENCES

- [1] N. González-Prelcic *et al.*, “The integrated sensing and communication revolution for 6G: Vision, techniques, and applications,” *Proc. IEEE*, vol. 112, no. 7, pp. 676–723, 2024.
- [2] S. Zhai, J. Fan, J. Gao, and G. Dai, “Multipath-based SLAM exploiting extended object estimation and classification,” *IEEE Trans. Wireless Commun.*, vol. 24, no. 8, pp. 7029–7045, 2025.
- [3] A. Karttunen *et al.*, “Towards semantic radio SLAM with landmark feature extraction in mmwave networks,” in *2025 IEEE 5th Int. Symp. Joint Commun. & Sensing (JC&S)*, 2025, pp. 1–6.
- [4] Y. Ge *et al.*, “Pilot-based end-to-end radio positioning and mapping for ISAC: Beyond point-based landmarks,” 2025. [Online]. Available: <https://arxiv.org/abs/2505.07402>
- [5] P. I. H. Karstensen *et al.*, “Bistatic radio SLAM with offline shape estimation,” in *2025 19th Eur. Conf. Antennas Propag. (EuCAP)*, 2025, pp. 1–5.
- [6] M. Baum and U. D. Hanebeck, “Extended object tracking with random hypersurface models,” *IEEE Trans. Aerosp. Electron. Syst.*, vol. 50, no. 1, pp. 149–159, 2014.

- [7] N. Wahlström and E. Özkan, "Extended target tracking using Gaussian processes," *IEEE Trans. Signal Process.*, vol. 63, no. 16, pp. 4165–4178, 2015.
- [8] C. E. Rasmussen and C. K. I. Williams, *Gaussian Processes for Machine Learning*. The MIT Press, 2006.
- [9] E. Rastorgueva-Foi *et al.*, "Millimeter-wave radio SLAM: End-to-end processing methods and experimental validation," *IEEE J. Sel. Areas Commun.*, vol. 42, no. 9, pp. 2550–2567, 2024.
- [10] A. Shahmansoori *et al.*, "Position and orientation estimation through millimeter-wave MIMO in 5G systems," *IEEE Trans. Wireless Commun.*, vol. 17, no. 3, pp. 1822–1835, 2018.
- [11] O. Kaltiokallio *et al.*, "Robust snapshot radio SLAM," *IEEE Trans. Veh. Technol.*, vol. 74, no. 5, pp. 8460–8465, 2025.
- [12] M. Ester *et al.*, "A density-based algorithm for discovering clusters in large spatial databases with noise," in *kdd*, vol. 96, no. 34, 1996, pp. 226–231.
- [13] NR; *Physical Channels and Modulation*, 3GPP Std. TS 38.211, Sep. 2023.